AAS 20-661

SPACE CARVING IN SPACE: A VISUAL-SLAM APPROACH TO 3D SHAPE RECONSTRUCTION OF A SMALL CELESTIAL BODY

Travis Driver[*], Mehregan Dor[†], Katherine A. Skinner[‡], Panagiotis Tsiotras[§]

Missions to small bodies typically involve an initial characterization phase, where a 3D shape model is constructed for the purposes of vision-based relative navigation and estimation of the dynamical properties of the body. Current state-of-the-practice methods for shape reconstruction, such as Stereophotoclinometry (SPC), rely heavily on human-in-the-loop processes executed on the ground, thus constraining the level of autonomy that can be achieved by these missions. This work details a visual simultaneous localization and mapping (VSLAM) based autonomous shape reconstruction algorithm for the estimation of the dynamical properties and for the construction of a preliminary shape model of a small celestial body. The proposed method is applied to both simulated and real image data and is shown to accurately reconstruct the 3D shape of the target asteroid.

INTRODUCTION AND RELATED WORK

With the recent increase in the number of missions to near-Earth asteroids and other small celestial bodies, such as JAXA's Hayabusa2 mission to Asteroid (162173) Ryugu[1] and NASA's OSIRIS-REx mission to Asteroid (10195) Bennu,[2] opportunities have emerged for research in autonomous algorithms for relative navigation and *in-situ* characterization of small bodies. Typically, these missions involve an initial extended characterization, where a 3D shape model of the small body is reconstructed incrementally from a sequence of images acquired during a controlled orbit around the body.[3] These shape models are then used to derive high-resolution digital terrain maps (DTMs) and detailed physical and dynamical property estimates of the small body. Moreover, DTMs can be correlated with images taken on-board the spacecraft to provide an accurate relative navigation solution.[3–5] However, current state-of-the-practice shape estimation methods rely heavily on support from the ground to achieve accurate results. This reliance on ground-based operations greatly limits the autonomous relative navigation capabilities of the spacecraft and introduces added time, complexity, and cost.

Stereophotoclinometry[4] (SPC) is the current method of choice for constructing detailed 3D shape models of small bodies for science objectives and relative navigation.[3,5,6] SPC estimates a collection of local topological landmark maps (L-maps) using estimated camera poses and Sun vector information along with pixel information from a set of surface features matched across multiple views. The L-maps are combined through an iterative optimization-based process to construct a

[*]PhD Student, Institute for Robotics and Intelligent Machines, School of Aerospace Engineering, Georgia Institute of Technology, Atlanta, GA 30313, USA.

[†]PhD Candidate, School of Aerospace Engineering, Georgia Institute of Technology, Atlanta, GA 30313, USA.

[‡]Postdoctoral Fellow, School of Aerospace Engineering, Georgia Institute of Technology, Atlanta, GA 30313, USA.

[§]David and Lewis Chair, Professor, Institute for Robotics and Intelligent Machines, School of Aerospace Engineering, Georgia Institute of Technology, Atlanta, GA 30313, USA.

global shape model of the body. While SPC is effective, it relies on a computationally intensive process that is executed completely off-board and offline, and requires human input from operators on the ground for the identification of robust surface features to match between images.

The development of more efficient and autonomous 3D reconstruction methods has been identified as a major factor for enabling future small body science missions, and has been the subject of previous related works. Bandyonadhyay et al.[7] and Baker et al.[8] present silhouette-based methods to estimate the shape of a small body from a set of images. Silhouette extraction typically involves estimating a contour between the foreground object and the background in an image using pixel information directly. While their shape reconstruction results are promising, both methods operate on the assumption that the Sun fully illuminates the target body in order to ensure accurate silhouette acquisition, and that the orientation and distance of the camera with respect to the small body is precisely known *a priori*. Additionally, Reference 7 assumes that the small body is performing pure rotation about its principal axis to simplify the rotation rate estimation process. However, accurate silhouettes are difficult to extract when shadowing and inconsistent illumination are present, which is very often the case in space-based imagery. Dor et al.[9] applies ORB-SLAM to the non-cooperative rendezvous problem for estimation of a feature map of a target satellite and the relative camera pose but does not reconstruct a volumetric representation of the object being mapped. Kulumani et al.[10] and Bercovici et al.[11] present shape reconstruction algorithms that rely on Light Detection And Ranging (LiDAR) measurements. In contrast, our method leverages images from optical cameras given their relatively low complexity, low power consumption, and ability to operate in a wide range of conditions.

Feature-based formulations[12–14] for 3D reconstruction that do not suffer from the same limitations as silhouette-based methods have also been proposed. These methods rely on feature points and camera poses estimated through visual simultaneous localization and mapping (VSLAM), or structure from motion (SfM), to construct a 3D model from the features through enforcing a set of free-space constraints between the points and the camera. Pan et al.[12] presents an online 3D reconstruction pipeline that tracks the relative pose of an object with respect to a fixed-position camera while also estimating its 3D shape. However the process is not incremental and starts over at each keyframe. Lovi et al.[13] exploits Parallel Tracking and Mapping (PTAM)[15] to *incrementally* reconstruct complex scenes online while simultaneously estimating the pose of the camera using a laptop CPU. More recently, Piazza et al.[14] demonstrated state-of-the-art incremental manifold reconstruction using the output of ORB-SLAM[16] on a challenging computer vision benchmark[17] operating in real-time on a single CPU core. These methods demonstrate impressive reconstruction results, and their ability to operate online on minimal hardware make them particularly attractive for autonomous small body characterization due to on-board computing constraints of spacecraft. For the proposed application, factors such as the large relative distance between the on-board camera and the target asteroid, dynamic lighting conditions, and repetitive surface textures can introduce outliers and significant noise in the feature point and camera pose estimates. While Reference 12 proposes a Gaussian noise model to account for possible noise, the method is only applied to examples with a relatively low noise profile. In this paper, we adopt a similar feature-based formulation to Reference 12 and illustrate it's effectiveness for *in-situ* 3D shape reconstruction of a small celestial body. Additionally, we propose a set of filtering algorithms in order to better compensate for outliers in the feature map and noise in the final shape model.

This work proposes a 3D shape reconstruction algorithm that leverages surface feature and camera pose estimates from a VSLAM system to estimate the physical properties and to construct a

preliminary shape model of a small celestial body. The shape reconstruction pipeline takes as input a set of non-uniform, noisy surface feature points and camera poses which are estimated from a collection of monocular images. To this end, feature-based monocular VSLAM is employed to simultaneously estimate the set of 3D feature points and the position and orientation of the camera from each image. The input from the VSLAM system provides free-space constraints for the proposed feature-based space carving approach to estimate the shape of the small body as a collection of non-uniform tetrahedral elements from the Delaunay triangulation of the feature map. A visualization of the shape reconstruction pipeline is shown in Figure 1. Our algorithm requires no strict assumptions on surface illumination, and the full 6DOF pose (position and orientation) of the camera is estimated through the VSLAM solution. The proposed algorithm is validated using simulated images of Asteroid (25143) Itokawa and real images of Asteroid (4) Vesta.

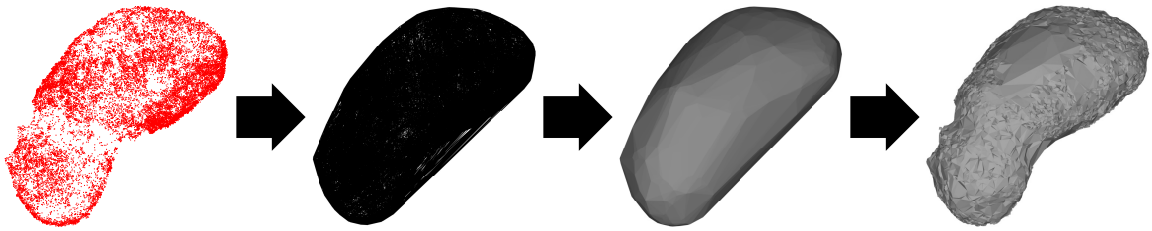

Figure 1: Summary of the shape reconstruction process (left to right): a set of surface features is input from the VSLAM system; the Delaunay triangulation of the points is computed; the triangulation defines the initial carving space (i.e., the convex hull of the points); free-space constraints are enforced to carve away tetrahedra outside the underlying volume to construct a 3D shape model.

VISUAL SIMULTANEOUS LOCALIZATION AND MAPPING

Our shape reconstruction algorithm relies on feature point and camera pose estimates from a feature-based monocular VSLAM system. Monocular VSLAM[18] leverages images captured from discrete viewpoints along the vehicle's trajectory to provide spatial information about the target scene, while simultaneously estimating the observer's ego-motion. As VSLAM algorithms[15,16] are commonly known and are not a main contribution of this paper, we only include a brief summary of the method used for our simulations in this section for completion.

The VSLAM architecture is comprised of two main components: the *front-end* and the *back-end*. Detection and tracking of salient surface features is performed by the front-end by first detecting image keypoints through computing Oriented FAST and Rotated BRIEF (ORB)[19] features, and then extracting their binary feature descriptors. The binary feature descriptors are then matched between frames using a brute force approach based on the Hamming distance, and the resulting correspondences are used to initialize the pose of the camera with the Perspective-n-Point (PnP) algorithm[20] and to initialize the 3D position of newly matched keypoints through triangulation. The data associations from the front-end are used to add factors to encode probabilistic constraints between the 3D feature point and the camera pose estimates in a *factor graph* in the back-end of the VSLAM system. Our VSLAM solution utilizes the Georgia Tech Smoothing and Mapping (GTSAM) factor graph framework[21,22] to formulate SLAM as a maximum *a posteriori* inference problem for estimation of the unknown variables (e.g., 3D feature point locations, camera pose) given a set of measurements (e.g., 2D keypoint locations) and the measurement model. The factor graph formulation of the SLAM problem is shown in Figure 2. Feature point locations and camera poses are estimated through *factor graph optimization* by solving a non-linear least-squares problem

in the back-end. The VSLAM pipeline also features *loop closure* to aid in reducing localization drift accumulated between successive local optimizations over the spacecraft's navigation sequence. To this end, a bag-of-words (BoW) image representation[23] is leveraged for place recognition, and similarity metrics between each image's BoW vectors are computed and compared to determine when to "close" detected loops by addition of a factor between the camera poses. Loop closure is an important component of the VSLAM system in the proposed framework, as it is expected that the spacecraft will experience multiple loop-closures in an orbital relative navigation scenario.

Currently, map and pose information from the VSLAM algorithm is optimized in an initial step and then used as input into the shape reconstruction component in a second phase. The relative pose between the spacecraft from two images in the sequence is used to rectify the scale ambiguity inherent to monocular VSLAM systems, and to allow for direct comparison of the final solution with ground truth data. Future work will focus on integrating the VSLAM and shape reconstruction algorithms into a single pipeline.

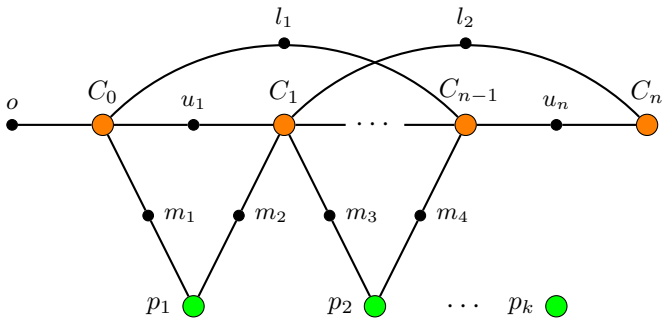

Figure 2: Factor graph formulation of the SLAM problem. Variable nodes are camera poses C and landmark (feature) positions p. Factor nodes are pose measurements u, landmark measurements m, loop closing constraints l, and possibly a prior factor o.

VORONOI DIAGRAM AND DELAUNAY TRIANGULATION

Voronoi diagrams (VD) and Delaunay triangulation (DT) are geometric data structures built upon the notion of nearness that will allow for the reformulation of the shape reconstruction problem as a *space carving* problem using the VSLAM feature map and pose solution. These data structures, along with a set of points sampled from a continuous surface, allow for complex geometries to be discretized as a collection of simplices (triangles in 2D and tetrahedrons in 3D). The following definitions are adopted from Dey.[24]

Let $\mathcal{P}$ be a set of affinely independent points in $\mathbb{R}^d$. The Voronoi cell V_p for each point $p \in \mathcal{P}$ is defined as[24]

$$V_p = \{x \in \mathbb{R}^d \mid d(x,p) \leq d(x,q), \forall\, q \in \mathcal{P}, q \neq p\}, \tag{1}$$

that is, V_p is the set of all points whose Euclidean distance $d(\cdot,\cdot)$ to p is smaller than the distance to any other point in $\mathcal{P}$. The Voronoi diagram $\text{Vor}(\mathcal{P})$ is defined as the *cell complex* of the Voronoi cells. Here, a cell complex is defined as a collection of polytopes that intersect in a face.[24] The Delaunay triangulation $\text{Del}(\mathcal{P})$ of $\mathcal{P}$ is the dual graph of $\text{Vor}(\mathcal{P})$ and is defined as[24]

$$\text{Del}(\mathcal{P}) = \{\sigma_{(d)} = \text{Conv}(T) \mid \bigcap_{p \in T \subseteq \mathcal{P}} V_p \neq \varnothing\}, \tag{2}$$

that is, $\text{Del}(\mathcal{P})$ partitions the convex hull of $\mathcal{P}$ into a complex of d-dimensional simplices such that their corresponding Voronoi cells have nonempty intersection. Here, the d-simplex $\sigma_{(d)} = \text{Conv}(T)$

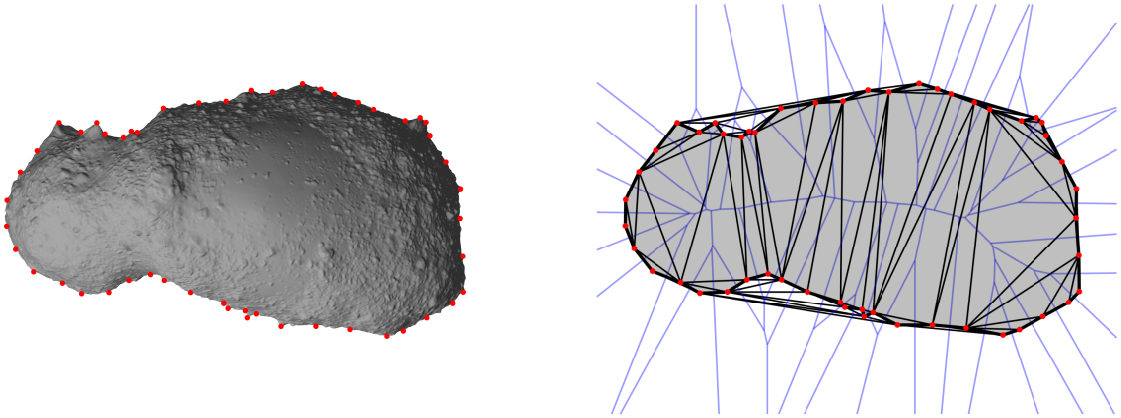

Figure 3: 2D illustration of the formulated space carving problem on Itokawa: (left) a set of features are sampled from the target asteroid's surface and (right) the underlying shape of the curve is reconstructed from the associated Delaunay triangulation (black lines) of the points by selecting a subset of the triangles. The Voronoi diagram of the point set is shown in blue.

is the convex hull of a set of $d+1$ affinely independent points $T \subseteq \mathcal{P}$. Every triangle (tetrahedron) in the Delaunay triangulation satisfies the empty circumscribing ball property, i.e., no point $p \in \mathcal{P}$ can lie in the circumscribing ball of a Delaunay triangle (tetrahedron).[24]

An important motivation for the use of Delaunay triangulation in the proposed 3D reconstruction algorithm is the following property: under the assumption that the sampling of $\mathcal{P}$ of the underlying surface is sufficiently dense, it can be shown that the facets and edges between sample points of the surface are contained within $\text{Del}(\mathcal{P})$.[25,26] Therefore, the Delaunay complex allows for the reformulation of the shape reconstruction problem as a *space carving* problem, i.e., determining a subset of simplices and their facets in $\text{Del}(\mathcal{P})$ that accurately approximate the underlying surface and shape of the object; this is illustrated in Figure 3. Another important motivation is that the construction of the VD and DT is inherently incremental and is therefore amenable to incremental optimization as new measurements are acquired by VSLAM.

3D SHAPE RECONSTRUCTION

The main contribution of this paper is the proposed shape reconstruction pipeline that utilizes our VSLAM solution. The shape reconstruction pipeline has three main components: (1) outlier detection of mapped feature points from the VSLAM solution through the use of a k-nearest neighbors graph (k-NNG), (2) probabilistic feature-based space carving for reconstruction of the object from the mapped feature points and their corresponding DT and visibility constraints, and (3) filtering of the carved model by employing basic morphological operations defined on the tetrahedra of the DT.

Outlier Detection

A k-NNG[27] is used to identify two main outlier types: (Type I) points in regions where the local point density is low relative to the mean point density of the map,[28] and (Type II) points whose mean viewing direction deviates from that of other points in some neighborhood. For Type I outliers, the mean distance from the point to its $k = 5$ nearest neighbors is computed, and the point is omitted from the reconstruction process if its mean k-NN distance is greater than a 1-σ deviation from the global mean of all points in the map. For Type II outliers, the mean direction of the visibility ray $r_{j,k}$

from the observed feature point p_k to the camera c_j is computed for each point and compared with that of it's $k = 5$ nearest neighbors. If, on average, the ray direction deviates from it's neighbors by more that $60°$, then the point is omitted from the reconstruction process. While this is a post-processing step in the current formulation, these simple geometric tests can easily be integrated into the VSLAM pipeline to select a subset of features that are amenable to the reconstruction method.

Probabilistic Feature-based Space Carving

In this work we adopt a probabilistic feature-based space-carving approach that uses 3D spatial information provided by the VSLAM system to carve away tetrahedra defined by the Delaunay triangulation based on free-space constraints between the point and the camera.[12] Space carving is the process of reconstructing 3D scenes from a set of images by enforcing a set of free-space constraints to "carve" out the scene from a larger volume in space, traditionally formulated as a silhouette-based technique.[29] The proposed feature-based approach is motivated by the assertion that *indirect* methods that extract a set of intermediate features (such as ORB keypoints and descriptors) from the image are typically more robust to lighting inconsistencies and large viewpoint changes than *direct methods* which operate on pixel intensities directly.[30]

To formulate the proposed solution, let $\mathcal{P} \subset \mathbb{R}^3$ denote the set of estimated feature points and let $\mathcal{C} \subset \mathbb{R}^3$ be the set of estimated camera positions. Furthermore, let $\mathcal{R}$ denote the set of all rays defined by $r_{j,k} = (p_k^T \quad m_{j,k}^T)^T \in \mathbb{R}^6$ from each feature point $p_k \in \mathcal{P}$ towards each camera $c_j \in \mathcal{C}$ from which it is visible, where $m_{j,k} = (c_j - p_k)/\|c_j - p_k\| \in \mathbb{R}^3$. Each triangular facet F_ℓ with vertices $\mathcal{V}_\ell \subset \mathcal{P}$ of the tetrahedra $T_i \in \text{Del}(\mathcal{P})$ is taken to be an estimate of an element of the underlying shape model (i.e., either on the surface or in the interior), and feature points p_k are assumed to be observations of a surface element corrupted by Gaussian noise along the ray $r_{j,k}$, centered at the surface of a facet F_ℓ with variance σ^2. We define the probability of the estimate F_ℓ given the ray $r_{j,k}$ from the observed feature point p_k to the camera c_j (see Figure 4) as follows, similar to Reference 12:

$$\mathbb{P}(F_\ell \mid r_{j,k}) = \begin{cases} \mathbb{P}(x \leq d_k), & \text{if } r_{j,k} \text{ intersects } F_\ell, \\ 1, & \text{otherwise,} \end{cases} \tag{3}$$

where $x \sim \mathcal{N}(0, \sigma^2)$ is the signed distance along $r_{j,k}$ (negative away from the camera) with $\mathbb{E}(x) = \bar{x} = 0$ defined as the intersection of $r_{j,k}$ and the facet F_ℓ, and d_k is the signed distance from $x = 0$ to point p_k of $r_{j,k}$. The Intersection between a ray $r_{j,k}$ and a triangular facet F_ℓ is computed according to Moller et al.[31]

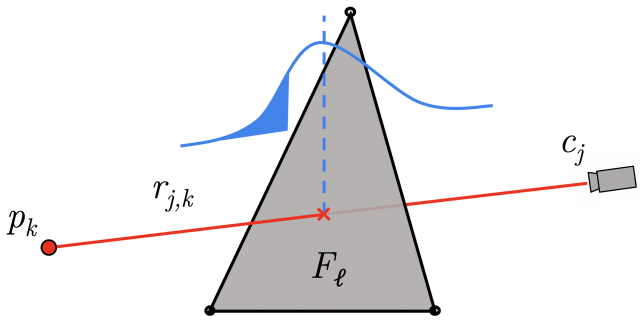

Figure 4: Proposed free-space constraint. The camera c_j observes a point p_k, but the the facet F_ℓ intersects the ray $r_{j,k}$ and would occlude the point.

Evaluating F_ℓ against all rays in $\mathcal{R}$, and further assuming that each observation is independent, gives

$$\mathbb{P}(F_\ell \mid \mathcal{R}) = \prod_{r_{j,k} \in \mathcal{R}} \mathbb{P}(F_\ell \mid r_{j,k}). \tag{4}$$

Furthermore, the probability $\mathbb{P}(T_i)$ of a tetrahedron $T_i \in \text{Del}(\mathcal{P})$ is defined as

$$\mathbb{P}(T_i) = \min\left(\left\{\mathbb{P}(F_1^{(i)} \mid \mathcal{R}), \ldots, \mathbb{P}(F_4^{(i)} \mid \mathcal{R})\right\}\right), \tag{5}$$

where $\left\{F_1^{(i)}, F_2^{(i)}, F_3^{(i)}, F_4^{(i)}\right\}$ are the faces of tetrahedron T_i. If $\mathbb{P}(T_i) < \eta$ for some threshold η (set to $\eta = 0.15$ for our experiments), then the tetrahedron is carved (marked as free-space) from $\text{Del}(\mathcal{P})$.

Morphological Filtering

The large relative distance between the on-board camera and the target asteroid and the dynamic lighting conditions inherent to the space environment can introduce significant noise in the feature points and camera pose estimates, which may not be properly compensated for by the probabilistic space carving method. Moreover, the relative motion of the spacecraft with respect to the small body is typically constrained in an orbital plane. This can limit the availability of novel viewpoints between successive revolutions, allowing for certain types of spurious features to persist in the carved model. Therefore, we define a set of filtering procedures using the formalism of morphological operations on the tetrahedra in the DT to compensate for these unique constraints.

Morphological operators are a special form of non-linear filters, and are primarily defined on pixels for filtering, segmentation, classification, and general analysis of 2D binary and gray-scale images.[32] An important insight is that the 3D partitioning of space and adjacency relationships defined by $\text{Del}(\mathcal{P})$ and $\text{Vor}(\mathcal{P})$ can be considered a 3D gray-scale image with tetrahedral elements and $\mathbb{P}(T_i) \in [0\ 1]$ as their respective "intensity" values. Therefore, the basic operations *erode* and *dilate* can be extended to operate on the tetrahedra and their respective probability computed in the previous feature-based space carving step.

Morphological operators are often based on predefined sets called *structuring elements*.[32] Let $\mathcal{E} \subseteq \mathbb{R}$ denote the space of gray-scale image values, and let $\mathcal{H}, \mathcal{G} \subseteq \mathbb{R}^3$ denote the domains of the 3D gray-scale image $h\colon \mathcal{H} \to \mathcal{E}$ and the 3D gray-scale structuring element $g\colon \mathcal{G} \to \mathcal{E}$, respectively. For our purposes, we will consider a structuring element that is both flat (i.e., $g(i,j,k) = 0$ for all $(i,j,k) \in \mathcal{G}$) and symmetric. Then the *dilation* of h by g is defined as[33]

$$(h \oplus g)(x,y,z) = \max_{(i,j,k) \in \mathcal{G}} \{h(x+i, y+j, z+k)\}, \tag{6}$$

for all $(x+i, y+j, z+k) \in \mathcal{H}$. That is, the elements in the dilated image $h \oplus g$ take the *maximum* value in a neighborhood defined by $\mathcal{G}$ of the elements in h. In a similar fashion, the *erosion* of h by g is defined as[33]

$$(h \ominus g)(x,y,z) = \min_{(i,j,k) \in \mathcal{G}} \{h(x+i, y+j, z+k)\}, \tag{7}$$

for all $(x+i, y+j, z+k) \in \mathcal{H}$. That is, the elements in the eroded image $h \ominus g$ take the *minimum* value in a neighborhood defined by $\mathcal{G}$ of the elements in h. The basic operations of erosion and

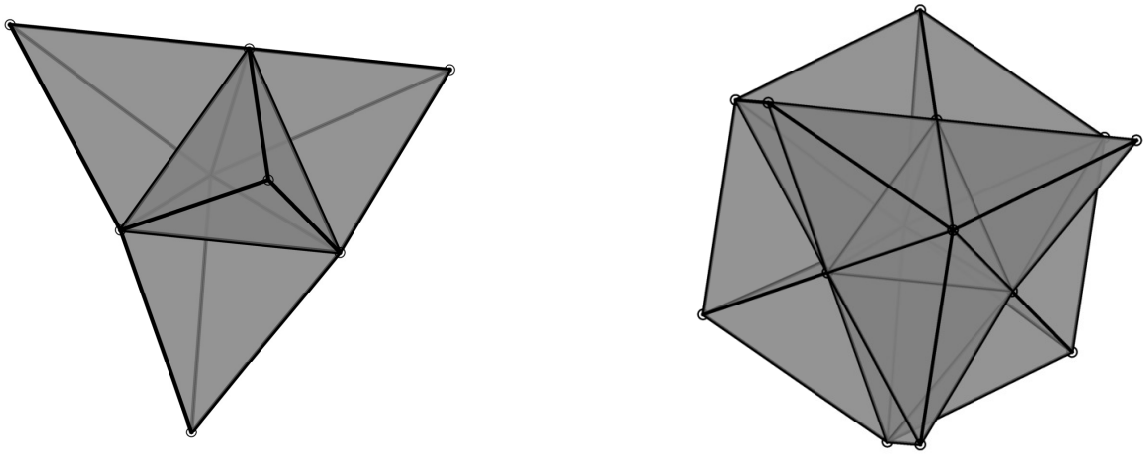

(a) $\mathcal{G}_1$ **(b)** $\mathcal{G}_2$

Figure 5: Example structuring elements.

dilation can be combined to form more complex operations such as *opening*. The opening operation is defined as an erosion operation followed by a dilation operation:[33]

$$h \circ g = (h \ominus g) \oplus g. \tag{8}$$

The opening operation is *idemponent* (i.e., converges in a single step) and *anti-extensive* (i.e., the result is smaller than the original image).[32,33]

For our purposes, we will utilize two different structuring elements. The first structuring element $\mathcal{G}_1$ is taken to be the set containing a tetrahedron, the *origin* of the structuring element denoted T_O, and its adjacent tetrahedra. Here, two tetrahedra T_i, T_j are considered to be *adjacent* if they intersect in a face. The second structuring element $\mathcal{G}_2$ is taken to be the set containing a tetrahedron T_O, all of the tetrahedra that are adjacent to the tetrahedron T_O, and additionally all of the tetrahedra that are adjacent to the tetrahedra that are adjacent to T_O. Examples of these structuring elements are shown in Figure 5.

The connectivity of the tetrahedra in $\text{Del}(\mathcal{P})$ is also leveraged to identify spurious features in the carved shape. A tetrahedron is identified as spurious if (1) it is occupied but is adjacent to three tetrahedra, or (2) it is occupied, is adjacent to two free tetrahedra, and it's aspect ratio is below a threshold α (taken to be $\alpha = 0.02$ for our experiments). Here, the aspect ratio of a tetrahedron is defined as the ratio of its inradius to its longest edge. The first case represents tetrahedra that are not well integrated into the underlying shape model, while the second case promotes isotropic faces on the surface of the shape model and handles tetrahedron that are generally too thin with respect to the viewing direction to be carved using the proposed free-space constraint.

First, the opening operation with the $\mathcal{G}_2$ structuring element is applied to the tetrahedra in the DT. Next, spurious features are identified and eliminated through an iterative conditional erosion step using the $\mathcal{G}_1$ structuring element and the defined criteria. For our simulations, this procedure was used in order to remove visual artifacts from the surface of the shape model and was also shown to decrease the relative error of the estimated physical parameters with respect to the theoretical values. An overview at each step of this process is shown in Figure 6.

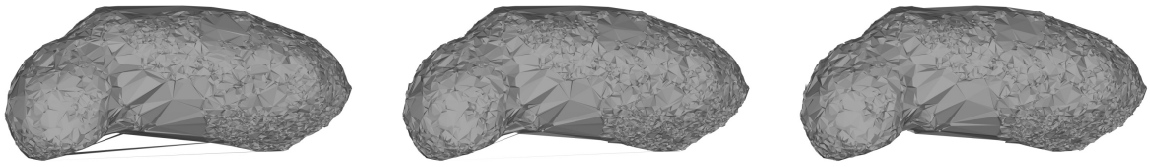

(a) Initial carving. **(b) Morphological opening.** **(c) Conditional erosion.**

Figure 6: Morphological filtering results.

EXPERIMENTAL SETUP

Both real images from the Dawn mission to Asteroid (4) Vesta and simulated images from the Hayabusa mission to Asteroid (25143) Itokawa were used to validate the proposed algorithm. These image sequences were chosen such that the majority of the surface of the asteroid was observed during the sequence and such that the spacecraft makes roughly one revolution with respect to a body-fixed frame of the asteroid without any large gaps in observations. Blender Cycles,[34] an open source ray tracing-based production renderer integrated in Blender, was used to generate photorealistic images of Itokawa using the high-resolution shape model provided by Gaskell et al.[35] The dataset of 100 simulated images used for our experiments were sampled using the ground truth mission parameters from the Hayabusa mission.[36] Camera parameters were set to match those of the Hayabusa Spacecraft Asteroid Multiband Imaging Camera (AMICA),[37] and images were synthesized using the theoretical camera pose and Sun pointing vector in a body-fixed frame of Itokawa at specified epochs during the Hayabusa mission taken from Saito et al.[38] A qualitative comparison between a real and simulated image is shown in Figure 7. During the sequence, the spacecraft makes roughly one revolution about the body with respect to a body-fixed frame of Itokawa at a mean radius of 8.0165 km from the origin. This simulated dataset will hereafter be referred to as `HAYAB`.

Moreover, real imagery[39] of Vesta acquired during the Rotation Characterization 3b (RC3b) observation phase of the Dawn mission was used to validate the algorithm. The images were captured

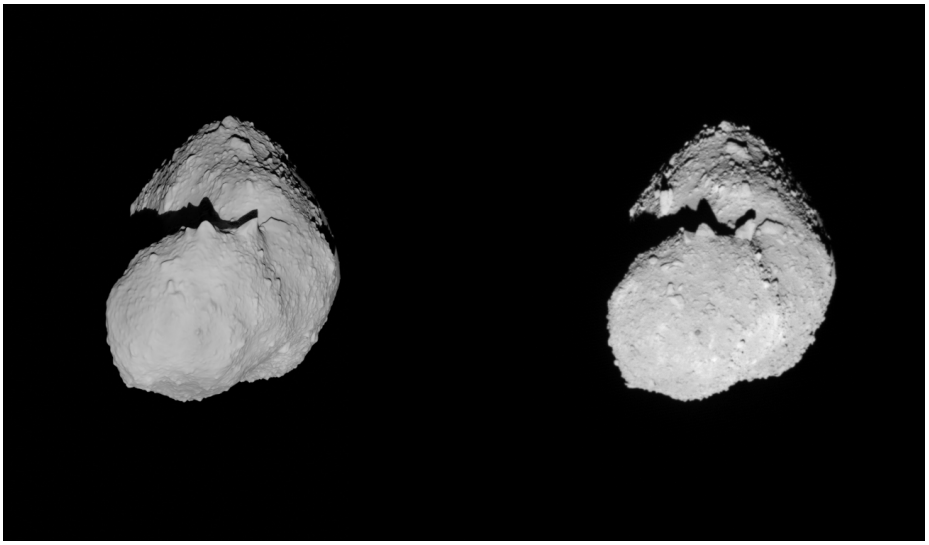

Figure 7: Simulated image (left) with real image[38] (right) of Asteroid (25143) Itokawa.

Table 1: Overview of Image sequences used for experiments.

Name	Mission	Target	Images	Mean Orbital Radius (km)	Size (pixels)	Resolution (km/pixel)
HAYAB	Hayabusa	(25143) Itokawa	100	8.0165	1024×1024	70×10^{-5}
DAWNRC3b	Dawn	(4) Vesta	64	5480.0	1024×1024	0.5

at a mean orbital radius of 5480.0 km, and the spacecraft makes roughly one revolution about the body with respect to a body-fixed frame. However, due to the downward spiraling trajectory of the orbit with respect to a body-fixed frame of Vesta, loop-closure constraints were not satisfied for any frame in this sequence. While a majority of the surface was imaged during the RC3b observation phase,[40] much of the surface of Vesta above latitude $60°N$ was occluded due to self-shadowing. Therefore, the northern polar region of the asteroid could not be reconstructed from this image sequence. This real dataset will henceforth be referred to as the DAWNRC3b sequence. Table 1 gives an overview of the two image sequences used for our experiments, and Figure 8 shows a sub-sampling of images from the respective datasets.

In addition, a *low-noise* case is presented using the HAYAB image sequence. This case serves to illustrate the effects of noise on the algorithm, and will also illustrate how the proposed morphological operations can help compensate for significant noise in the final solution. For this case only, the spacecraft relative pose was assumed known, and the resulting feature map from our VSLAM algorithm was filtered with respect to the theoretical shape model.[35] This scenario will be referred to as HAYAB,low-noise in the subsequent analysis.

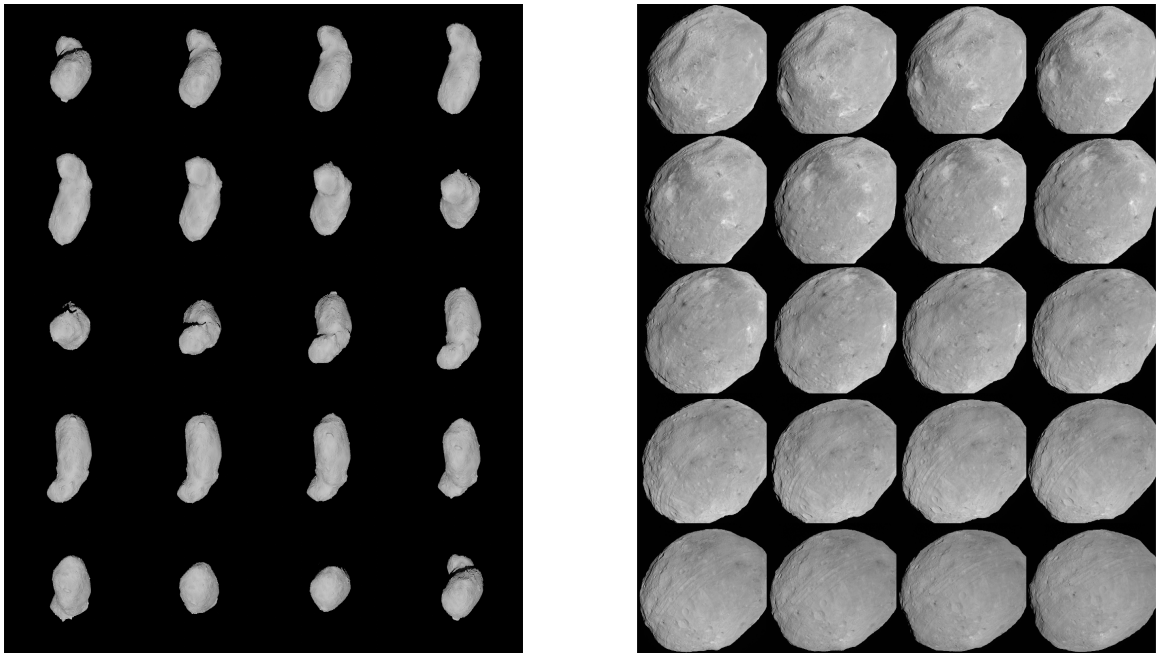

(a) HAYAB **(b) DAWNRC3b**

Figure 8: 20 sample images from the respective sequences.

RESULTS

Camera Pose and Feature Map Reconstruction

The reconstructed pose of the camera and feature map solution from the VSLAM pipeline for the respective experiments is shown in Figure 9. Points marked as `carved` include landmarks that were identified as outliers, that have corresponding tetrahedra that were eliminated as part of the reconstruction process, or that are interior points not included as vertices of the final surface mesh. The camera axes are shown at evenly spaced intervals with the x-axis in red, y-axis in green, and z-axis (boresight) in blue. The camera poses used to rectify the scale ambiguity of the monocular VSLAM system were given in a body-fixed frame of the respective asteroids. Therefore, all values reported are with respect to these frames. For `HAYAB`, the body-fixed frame of Itokawa is defined by its principal axes of inertia (assuming a uniform density) with the $x-$axis along the smallest moment of inertia, the $z-$axis along the largest moment of inertia, and the $y-$axis along the intermediate moment of inertia with its center of mass (CoM) as the origin.[41] For `RB3b`, the Claudia crater defines the prime meridian and the largest moment of inertia defines the z-axis, with the CoM (assuming a uniform density) located at $(-0.333, -1.409, -0.003)$ km relative to the origin.[42] Relative error magnitudes between the reconstructed and actual position and orientation of the camera are given in Table 2. The relative position error magnitude Δr is taken to be $\Delta r = \|r - r'\|$, where $r \in \mathbb{R}^3$ is the actual position of the camera with respect to the asteroid and $r' \in \mathbb{R}^3$ is the estimated position. We adopt an axis-angle representation to compute the relative angular error magnitude $\Delta\theta$ between R_{CA}, the actual orientation of the camera frame C with respect to the asteroid body-fixed frame A, and $R_{C'A}$, the estimated orientation of the camera frame C' with respect to A:[43]

$$\Delta\theta(R) = \cos^{-1}\left(\frac{\text{trace}(R) - 1}{2}\right), \quad R = R_{C'C} = R_{C'A}R_{CA}^T. \tag{9}$$

Table 2: VSLAM estimation results for the position and orientation of the camera. Relative error percentages are with respect to the mean orbital radius of the respective experiments.

	Δr (km)			$\Delta\theta$ (rad)		
	`max`	`mean`	`RMS`	`max`	`mean`	`RMS`
`HAYAB`	0.1448 (1.81%)	0.0816 (1.02%)	0.0859 (1.07%)	0.0237	0.0136	0.0145
`RC3b`	47.369 (0.86%)	23.079 (0.42%)	25.050 (0.46%)	0.0089	0.0049	0.0053

3D Shape Reconstruction and Physical Properties Estimation

In this section we will present the results of the proposed reconstruction method for the estimation of the physical properties (e.g., volume, principal moments of inertia) and 3D shape of a small celestial body. For the `HAYAB`, `low-noise` and `HAYAB` experiments, σ was taken to be 0.03 km, and for the `DAWNRC3b` experiment, σ was taken to be 10.00 km. A qualitative comparison between the final shape model from the proposed shape reconstruction pipeline and the theoretical shape models of Asteroids Itokawa[35] and Vesta[44] is shown in Figure 10. The theoretical shape model of Itokawa is taken to be the truth, as the simulated images of Itokawa in the `HAYAB` sequence were

Table 3: Relevant physical properties of the reconstructed shape model as compared to theoretical values. The normalized principal moments of inertia I_{xx}/M, I_{yy}/M, and I_{zz}/M are expressed with respect to the reference frame defined by the principal axes and CoM. The value reported for principal axes is the relative error with respect to the theoretical principal axes matrix computed using Equation 9. The experimental section reports two values, `<initial carving result>` → `<final filtered result>`.

	experimental	theoretical
	`HAYAB,low-noise`	
Volume $\left(\text{km}^3\right)$	1.82×10^{-2} (2.25%) → 1.80×10^{-2} (1.12%)	1.78×10^{-2}
I_{xx}/M $\left(\text{km}^2\right)$	0.642×10^{-2} (0.78%) → 0.636×10^{-2} (0.16%)	0.637×10^{-2}
I_{yy}/M $\left(\text{km}^2\right)$	2.154×10^{-2} (1.51%) → 2.145×10^{-2} (1.08%)	2.122×10^{-2}
I_{zz}/M $\left(\text{km}^2\right)$	2.267×10^{-2} (1.43%) → 2.259×10^{-2} (1.07%)	2.235×10^{-2}
λ	0.93 (0.00%) → 0.93 (0.00%)	0.93
Bounding box (km)	$0.5675 \times 0.3096 \times 0.2423 \rightarrow 0.5675 \times 0.3096 \times 0.2423$	$0.5558 \times 0.3027 \times 0.2430$
CoM (m)	$(0.542, 0.145, 0.920) \rightarrow (0.159, 0.091, 1.038)$	$(0.000, 0.000, 0.000)$
Principal axes (rad)	$0.0511 \rightarrow 0.0518$	0.0000
	`HAYAB`	
Volume $\left(\text{km}^3\right)$	1.85×10^{-2} (3.93%) → 1.79×10^{-2} (0.56%)	1.78×10^{-2}
I_{xx}/M $\left(\text{km}^2\right)$	0.652×10^{-2} (2.35%) → 0.638×10^{-2} (0.16%)	0.637×10^{-2}
I_{yy}/M $\left(\text{km}^2\right)$	2.169×10^{-2} (2.21%) → 2.145×10^{-2} (1.08%)	2.122×10^{-2}
I_{zz}/M $\left(\text{km}^2\right)$	2.289×10^{-2} (2.42%) → 2.268×10^{-2} (1.48%)	2.235×10^{-2}
λ	0.93 (0.00%) → 0.92 (1.08%)	0.93
Bounding box (km)	$0.5778 \times 0.3177 \times 0.2372 \rightarrow 0.5762 \times 0.3141 \times 0.2372$	$0.5558 \times 0.3027 \times 0.2430$
CoM (m)	$(-10.112, -0.639, 6.465) \rightarrow (-10.857, -0.839, 6.682)$	$(0.0000, 0.0000, 0.0000)$
Principal axes (rad)	$0.0508 \rightarrow 0.0519$	0.0000
	`DAWNRC3b`	
Volume $\left(\text{km}^3\right)$	7.43×10^7 (0.80%) → 7.34×10^7 (2.00%)	7.49×10^7
I_{xx}/M $\left(\text{km}^2\right)$	2.553×10^4 (0.66%) → 2.53×10^4 (1.44%)	2.570×10^4
I_{yy}/M $\left(\text{km}^2\right)$	2.620×10^4 (1.24%) → 2.601×10^4 (1.96%)	2.653×10^4
I_{zz}/M $\left(\text{km}^2\right)$	3.243×10^4(2.50%) → 3.227×10^4(1.99%)	3.164×10^4
λ	0.10 (28.57%) → 0.10 (28.57%)	0.14
Bounding box (km)	$572.24 \times 574.84 \times 431.44 \rightarrow 569.33 \times 573.41 \times 430.95$	$562.86 \times 568.18 \times 466.00$
CoM (km)	$(1.3190, -0.4150, -1.9610) \rightarrow (1.2230, -0.4930, -1.7520)$	$(0.0000, 0.0000, 0.0000)$
Principal axes	$0.0277 \rightarrow 0.0221$	0.0000

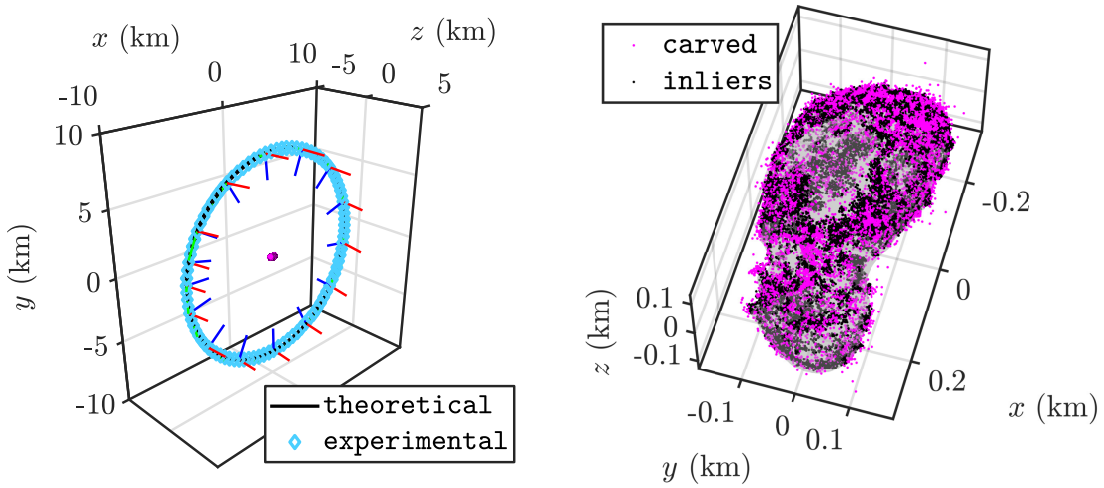

(a) HAYAB

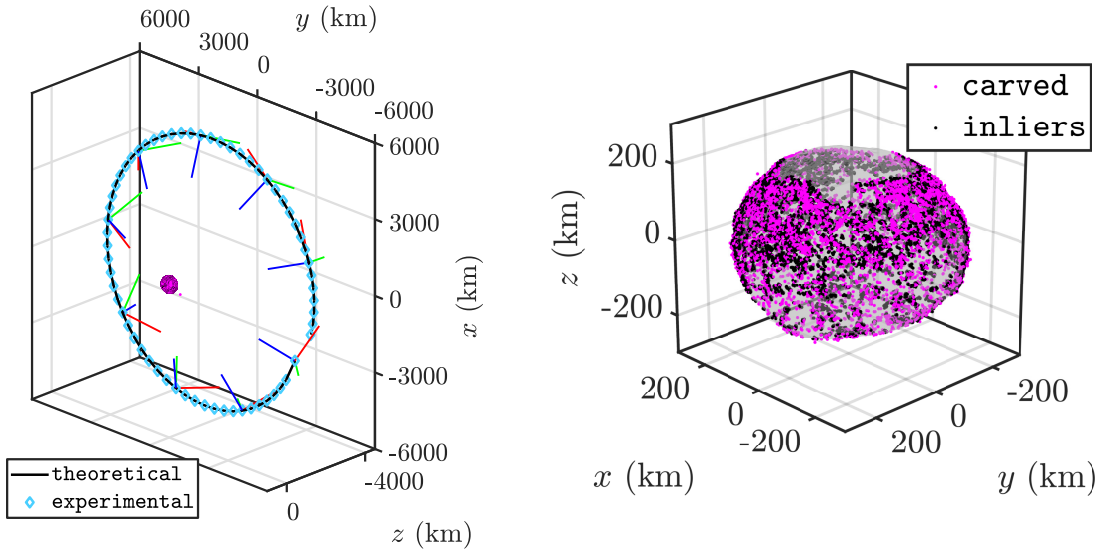

(b) DAWNRC3b

Figure 9: VSLAM pose and feature map estimation results in a body-fixed frame.

synthesized using this model. These results illustrate how the estimated shape model responds to feature maps with different noise profiles.

Table 3 reports a set of physical properties derived from the estimated shape model as compared to the theoretical values, including a simple measure of the mass distribution and the second degree and order gravity coefficients contained in the parameter λ defined as[45]

$$\lambda = \frac{I_{yy} - I_{xx}}{I_{zz} - I_{xx}} = \frac{4C_{22}}{C_{20} - 2C_{22}}. \tag{10}$$

The normalized principal moments of inertia I_{xx}/M, I_{yy}/M, and I_{zz}/M were computed assuming a uniform density throughout and are expressed with respect to a reference frame defined by the principal axes and CoM. The estimated physical properties are provided for both the initial space-

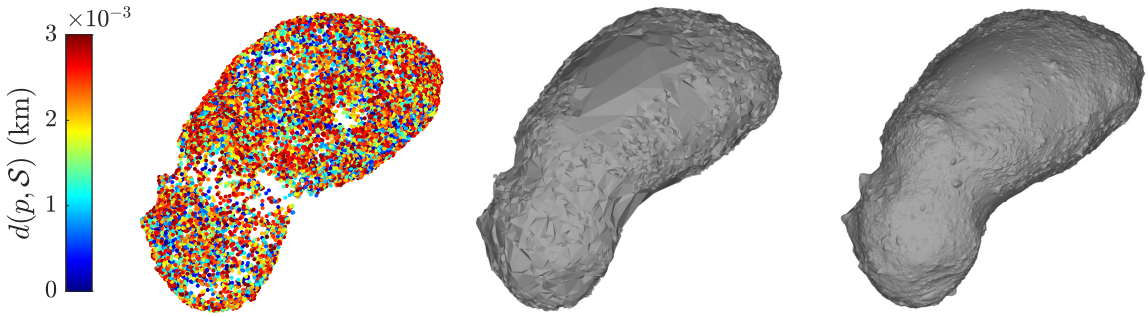

(a) `HAYAB`, `low-noise` (24383 points).

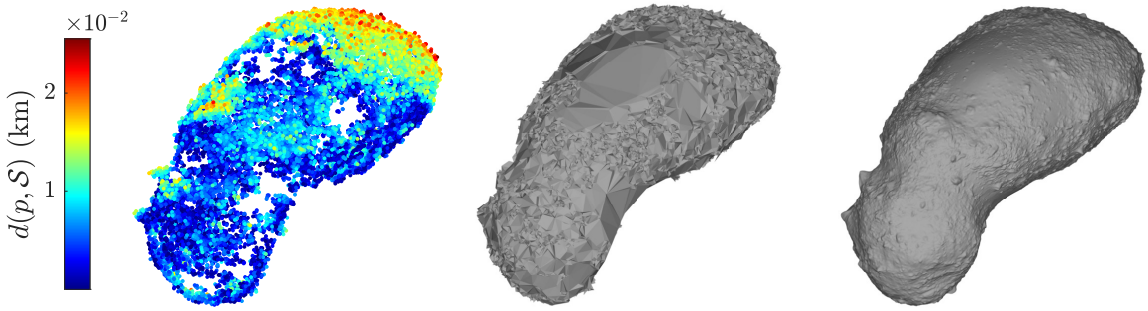

(b) `HAYAB` (27280 points).

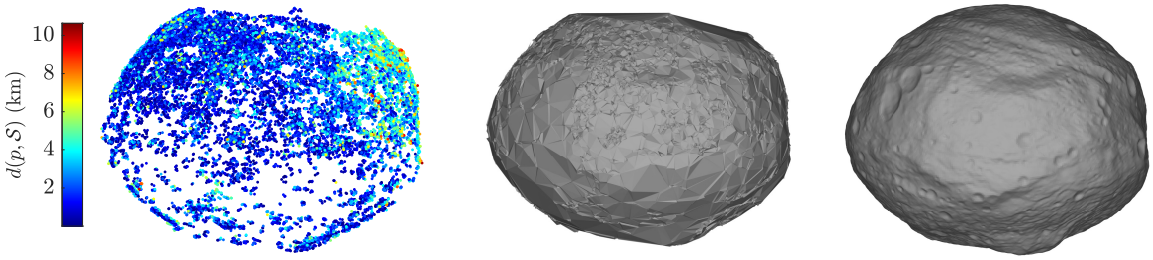

(c) `DAWNRC3b` (29203 points).

Figure 10: Qualitative comparison between the reconstructed feature map (left) and our reconstructed shape model (middle), and the theoretical shape model (right) for the various experiments. Feature points p are colorized by their distance $d(p, \mathcal{S})$ to the closest point on the theoretical surface mesh $\mathcal{S}$.

carving and the final filtered result to demonstrate the effects of the proposed morphological filtering procedure. In general, all estimates are improved by the procedure. The physical property values of Itokawa reported by Scheeres et al.[41] were taken to be the theoretical values for the HAYAB simulation and are provided in Table 3. The theoretical shape model[44] of Vesta was used to derive the theoretical values reported in Table 3, assuming constant density, and are within the reported error bounds of the values reported by Konopliv et al.[42] and Russell et al.[40] The presented results show close agreement between the reconstructed values from the proposed shape reconstruction algorithm and the theoretical values. In addition, we employ the well-known bidirectional Hausdorff distance d_H, detailed in Appendix A, to obtain a distance metric between the actual triangular surface mesh and the result obtained from our shape reconstruction algorithm. These results are summarized in Table 4 and Figure 11.

For the DAWNRC3b experiment, the filtering process can be seen to marginally increase the relative error for the estimates of I_{xx}/M, I_{yy}/M, and the volume. This is likely due to the fact that much of the surface of Vesta above latitude $60^\circ N$ was not mapped due to persistent self-shadowing during the image sequence. This presumably resulted in spurious tetrahedra in the north polar region of the carved shape model that were removed during the filtering process. However, the normalized principal moment of inertia I_{zz}/M estimate was improved as the model was more completely developed with respect to the z-axis. This lack of observations of the north polar region also likely inflated the values for DAWNRC3b reported in Table 4.

Baker et al.[8] provides estimates of geometric properties for the case of Itokawa that we will compare directly to our HAYAB experiment. The computed volume and bounding box of our reconstructed shape model (1.79×10^{-2} km^3 and $0.5762 \times 0.3141 \times 0.2372$ km, respectively) are much closer to the actual values (1.78×10^{-2} km^3 and $0.5558 \times 0.3027 \times 0.2430$ km, respectively) than the values reported in Reference 8 (2.045×10^{-2} km^3 and $0.5835 \times 0.2588 \times 0.3412$ km, respectively). Furthermore, the mean of the magnitudes of the Hausdorff distance values from our method (5.992×10^{-3} km) are almost an order of magnitude better (1.903×10^{-2}), and without making the same set of restrictive assumptions such as the Sun directly behind the camera and the camera position and orientation exactly known *a priori*. The detailed results show that our method is able to reconstruct an accurate volumetric model of the asteroids at a relatively large radial distance from the body by leveraging noisy feature point and camera pose estimates without making any strict assumptions on the surface illumination conditions of the target.

Table 4: Hausdorff distance $d_H(\mathcal{S}, \mathcal{S}')$, mean Hausdorff distance $d_H^{\mu}(\mathcal{S}, \mathcal{S}')$, and root mean square Hausdorff distance $d_H^{RMS}(\mathcal{S}, \mathcal{S}')$ between the theoretical surface mesh $\mathcal{S}$ and the surface mesh obtained from our shape reconstruction algorithm $\mathcal{S}'$. Relative error percentages are with respect to the bounding box diagonal of the respective theoretical shape models.

	$d_H(\mathcal{S}, \mathcal{S}')$ (km)	$d_H^{\mu}(\mathcal{S}, \mathcal{S}')$ (km)	$d_H^{RMS}(\mathcal{S}, \mathcal{S}')$ (km)
HAYAB3, ideal	9.240×10^{-3} (1.36%)	1.456×10^{-3} (0.21%)	1.786×10^{-3} (0.26%)
HAYAB3	2.321×10^{-2} (3.42%)	5.992×10^{-3} (0.88%)	7.237×10^{-3} (1.07%)
DAWNRC3b	37.273 (4.03%)	3.400 (0.37%)	6.560 (0.71%)

CONCLUSION

In this paper, we presented a 3D shape reconstruction algorithm that leverages feature point and camera pose estimates from a VSLAM system for reconstructing a preliminary shape model and

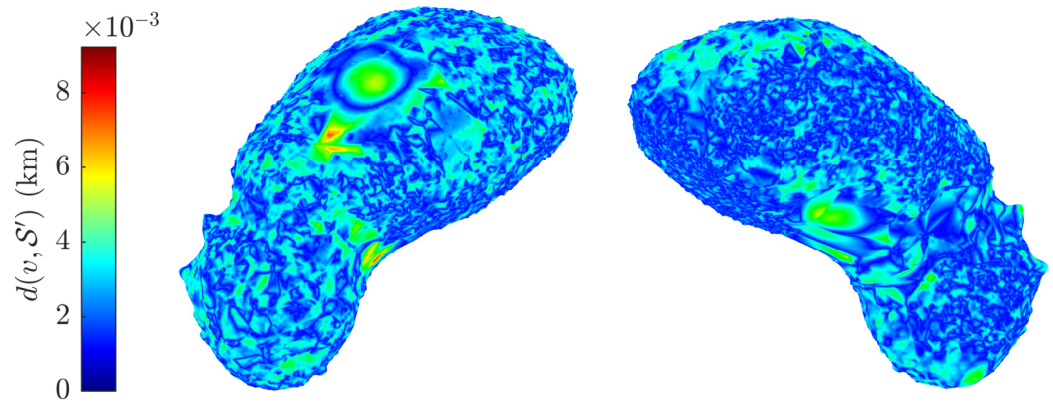

(a) `HAYAB, low-noise`

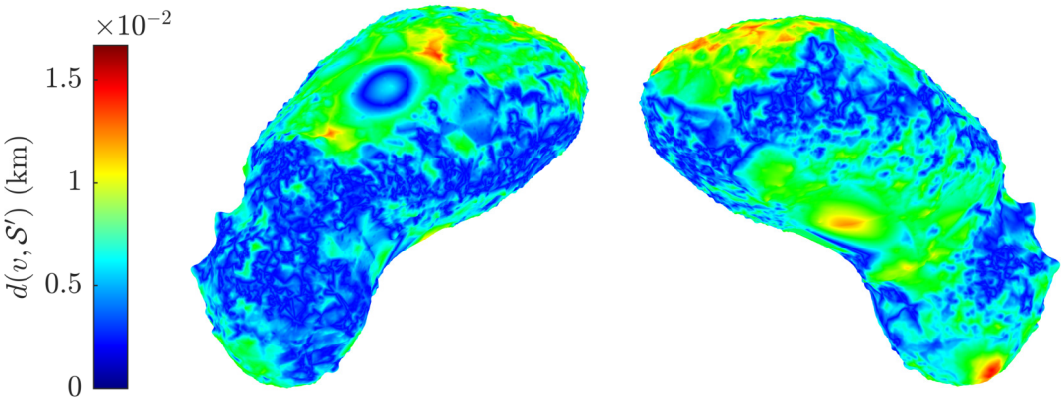

(b) `HAYAB`

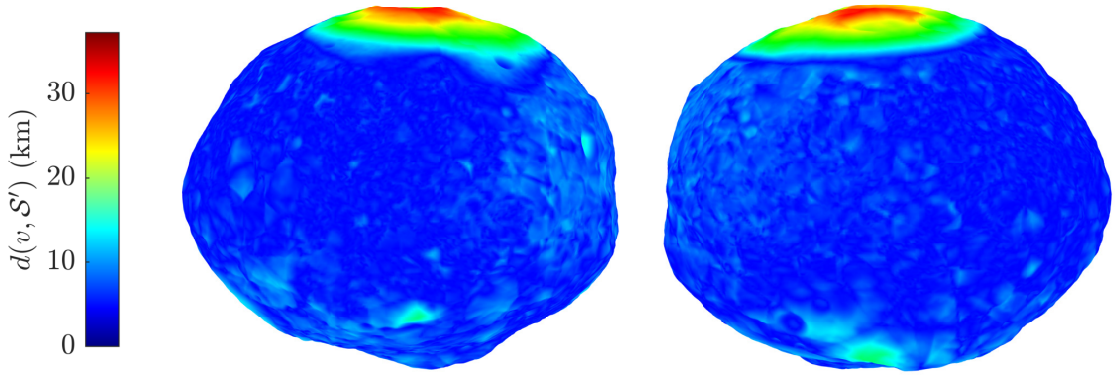

(c) `DAWNRC3b`

Figure 11: Distance $d(v, \mathcal{S}')$ from the vertices v of the theoretical shape model to the closest point on the triangular surface mesh $\mathcal{S}'$ obtained from our space carving algorithm overlaid on the theoretical shape model for visualization.

a set of physical properties of a small body during a relative navigation scenario. Our algorithm requires no strict assumptions on surface illumination and estimates the 3D shape of the small body. Moreover, the presented results demonstrate that our algorithm is able to accurately reconstruct the shape of the small body from noisy feature point and camera pose estimates from both simulated and real images through VSLAM. Future work will focus on integrating the shape reconstruction algorithm into a VSLAM pipeline that can operate online.

ACKNOWLEDGEMENT

This research was supported by the NASA Early Stage Innovations Grant 80NSSC18K0251.

REFERENCES

[1] Y. Tsuda, M. Yoshikawa, M. Abe, H. Minamino, and S. Nakazawa, "System design of the Hayabusa 2—Asteroid sample return mission to 1999 JU3," *Acta Astronautica*, Vol. 91, 2013, pp. 356–362.

[2] M. Nolan, C. Magri, E. Howell, L. Benner, J. Giorgini, C. Hergenrother, S. Hudson, D. Lauretta, J.-L. Margot, S. Ostro, and D. Scheeres, "Shape model and surface properties of the OSIRIS-REx target Asteroid (101955) Bennu from radar and lightcurve observations," *Icarus*, Vol. 226, 2013, pp. 629–640.

[3] S. Bhaskaran, S. Nandi, S. Broschart, M. Wallace, L. A. Cangahuala, and C. 0lson, "Small Body Landings Using Autonomous Onboard Optical Navigation," *J. of the Astronautical Sciences*, Vol. 58, No. 3, 2011, pp. 1365–1378.

[4] R. Gaskell, O. Barnouin-Jha, D. Scheeres, A. Konopliv, T. Mukai, S. Abe, J. Saito, M. Ishiguro, T. Kubota, T. Hashimoto, J. Kawaguchi, M. Yoshikawa, K. Shirakawa, T. Kominato, N. Hirata, and H. Demura, "Characterizing and navigating small bodies with imaging data," *Meteoritics & Planetary Science*, Vol. 43, No. 6, 2008, pp. 1049–1061.

[5] D. A. Lorenz, R. Olds, A. May, C. Mario, M. E. Perry, E. E. Palmer, and M. Daly, "Lessons learned from OSIRIS-REx autonomous navigation using natural feature tracking," *IEEE Aerospace Conference*, Big Sky, MT, USA, 2017, pp. 1–12.

[6] R. P. d. Santayana, M. Lauer, P. Muñoz, and F. Castellini, "Surface Characterization and Optical Navigation at the Rosetta Flyby of Asteroid Lutetia," *24th ISSFD*, Laurel, MD, USA, 2014.

[7] S. Bandyonadhyay, I. Nesnas, S. Bhaskaran, B. Hockman, and B. Morrell, "Silhouette-Based 3D Shape Reconstruction of a Small Body from a Spacecraft," *IEEE Aerospace Conference*, Big Sky, MT, USA, 2019, pp. 1–13.

[8] D. A. Baker and J. W. McMahon, "Limb-Based Shape Modeling: A Demonstration on Itokawa," *2nd RPI Space Imaging Workshop*, Saratoga Springs, NY, USA, 2019.

[9] M. Dor and P. Tsiotras, "ORB-SLAM Applied to Spacecraft Non-Cooperative Rendezvous," *AIAA SciTech Forum*, Kissimmee, FL, USA, 2018.

[10] S. Bandyonadhyay, I. Nesnas, S. Bhaskaran, B. Hockman, and B. Morrell, "Real Time Adaptive Shape Reconstruction for Asteroid Landing," *AAS/AIAA Astrodynamics Specialist Conference*, Snowbird, UT, USA, 2018.

[11] B. Bercovici and J. W. McMahon, "Robust Autonomous Small-Body Shape Reconstruction and Relative Navigation Using Range Images," *J. of Guidance, Control, and Dynamics*, Vol. 42, No. 7, 2019, pp. 1473–1488.

[12] Q. Pan, G. Reitmayr, and T. Drummond, "ProFORMA: Probabilistic Feature-based On-line Rapid Model Acquisition," *British Machine Vision Conference (BMVC)*, Dundee, UK, 2009.

[13] D. Lovi, N. Birkbeck, D. Cobza, and M. Jägersand, "Incremental Free-Space Carving for Real-Time 3D Reconstruction," *3D Data Processing, Visualization, and Transmission*, Paris, France, 2010.

[14] E. Piazza, A. Romanoni, and M. Matteucci, "Real-Time CPU-Based Large-Scale Three-Dimensional Mesh Reconstruction," *IEEE Robotics and Automation Letters*, Vol. 3, No. 3, 2018, pp. 1584–1591.

[15] G. Klein and D. Murray, "Parallel Tracking and Mapping for Small AR Workspaces," *Proc. Sixth IEEE and ACM International Symposium on Mixed and Augmented Reality (ISMAR'07)*, Nara, Japan, 2007.

[16] R. Mur-Artal, J. M. M. Montiel, and J. D. Tardos, "ORB-SLAM: A Versatile and Accurate Monocular SLAM System," *IEEE Transactions on Robotics*, Vol. 31, No. 5, 2015, p. 1147–1163.

[17] A. Geiger, P. Lenz, C. Stiller, and R. Urtasun, "Vision meets Robotics: The KITTI Dataset," *Intl. J. of Robotics Research (IJRR)*, 2013.

[18] C. Cadena, L. Carlone, H. Carrillo, Y. Latif, D. Scaramuzza, J. Neira, I. Reid, and J. Leonard, "Past, Present, and Future of Simultaneous Localization And Mapping: Towards the Robust-Perception Age," *IEEE Trans. on Robotics*, Vol. 32, No. 6, 2016, p. 1309–1332.

[19] E. Rublee, V. Rabaud, K. Konolige, and G. Bradski, "ORB: An Efficient Alternative to SIFT or SURF," *Intl. Conf. on Computer Vision (ICCV)*, Barcelona, Spain, 2011, pp. 2564–2571.

[20] V. Lepetit, F. Moreno-Noguer, and P. Fua, "EPnP: An accurate $O(n)$ solution to the PnP problem," *Intl. J. of Computer Vision*, Vol. 81, 2009.

[21] M. Kaess, H. Johannsson, R. Roberts, V. Ila, J. Leonard, and F. Dellaert, "iSAM2: Incremental Smoothing and Mapping Using the Bayes Tree," *Intl. J. of Robotics Research (IJRR)*, Vol. 31, No. 2, 2012, pp. 217–236.

[22] F. Dellaert, *Factor Graphs and GTSAM: A Hands-on Introduction*. Georgia Institute of Technology, 2012.

[23] D. Gálvez-López and J. D. Tardós, "Bags of Binary Words for Fast Place Recognition in Image Sequences," *IEEE Transactions on Robotics*, Vol. 28, No. 5, 2012, pp. 1188–1197.

[24] T. K. Dey, *Curve and Surface Reconstruction: Algorithms with Mathematical Analysis*. Cambridge Monographs on Applied and Computational Mathematics, Cambridge University Press, 2006.

[25] N. Amenta and M. Bern, "Surface Reconstruction by Voronoi Filtering," *Discrete & Computational Geometry*, Vol. 22, 1999, pp. 481–504.

[26] N. Amenta, S. Choi, T. K. Dey, and N. Leekha, "A Simple Algorithm for Homeomorphic Surface Reconstruction," *16^{th} Annual Symposium on Computational Geometry*, SCG '00, New York, NY, USA, Association for Computing Machinery, 2000, p. 213–222.

[27] D. Eppstein, M. Paterson, and F. Yao, "On nearest-neighbors graphs," *Discrete Computational Geometry*, Vol. 7, 1997, pp. 263–282.

[28] M. M. Breunig, H.-P. Kriegel, R. T. Ng, and J. Sander, "LOF: Identifying Density-Based Local Outliers," *Proceedings of the 2000 ACM SIGMOD International Conference on Management of Data*, SIGMOD '00, New York, NY, USA, Association for Computing Machinery, 2000, p. 93–104.

[29] K. Kutulakos and S. Seitz, "A Theory of Shape by Space Carving," *Intl. J. of Computer Vision*, Vol. 38, No. 3, 2000, pp. 199–218.

[30] N. Yang, R. Wang, X. Gao, and D. Cremers, "Challenges in Monocular Visual Odometry: Photometric Calibration, Motion Bias, and Rolling Shutter Effect," *IEEE Robotics and Automation Letters*, Vol. 3, No. 4, 2018, pp. 2878–2885.

[31] T. Möller and B. Trumbore, "Fast, minimum storage ray-triangle intersection," *J. of Graphics Tools*, Vol. 2, No. 1, 1997, pp. 21–28.

[32] L. Najman and H. Talbot, *Mathematical Morphology: from Theory to Applications*. Cambridge Monographs on Applied and Computational Mathematics, ISTE-Wiley, 2010.

[33] F. Shih, *Image Processing and Mathematical Morphology: Fundamentals and Applications*. CRC Press, 2009.

[34] B. O. Community, *Blender - a 3D modelling and rendering package*. Blender Foundation, Stichting Blender Foundation, Amsterdam, Netherlands, 2018.

[35] R. Gaskell, J. Saito, M. Ishiguro, T. Kubota, T. Hashimoto, N. Hirata, S. Abe, O. Barnouin-Jha, , and D. Scheeres, *Gaskell Itokawa Shape Model V1.0. HAY-A-AMICA-5-ITOKAWASHAPE-V1.0*. NASA Planetary Data System, 2008.

[36] A. Fujiwara, J. Kawaguchi, D. Yeomans, M. Abe, T. Mukai, T. Okada, J. Saito, H. Yano, M. Yoshikawa, D. Scheeres, O. Barnouin, A. Cheng, H. Demura, R. Gaskell, N. Hirata, H. Ikeda, T. Kominato, H. Miyamoto, A. Nakamura, and K. Uesugi, "The Rubble-Pile Asteroid Itokawa as Observed by Hayabusa," *Science*, Vol. 312, No. 5778, 2006, pp. 1330–1334.

[37] M. Ishiguro, R. Nakamura, D. J. Tholen, N. Hirata, H. Demura, E. Nemoto, A. M. Nakamura, Y. Higuchi, A. Sogame, A. Yamamoto, and e. al., "The Hayabusa Spacecraft Asteroid Multi-band Imaging Camera (AMICA)," *Icarus*, Vol. 207, No. 2, 2010, p. 714–731.

[38] J. Saito, T. Nakamura, H. Akiyama, H.and Demura, B. Dermawan, M. Furuya, T. Fuse, R. Gaskell, T. Hashimoto, Y. Higuchi, K. Hiraoka, N. Hirata, C. Honda, T. Honda, M. Ishiguro, K. Kitazato, S. Kobayashi, T. Kubota, N. Matsumoto, T. Michikami, H. Miyamoto, A. Nakamura, R. Nakamura, E. Nemoto, S. Sasaki, C. Shinohara, P. Smith, A. Sogame, J. Terazono, D. Tholen, A. Yamamoto, Y. Yokota, F. Yoshida, and A. Yukishita, *Hayabusa AMICA V1.0. HAY-A-AMICA-3-HAYAMICA-V1.0*. NASA Planetary Data System, 2010.

[39] A. Nathues, H. Sierks, P. Gutierrez-Marques, S. Schroeder, T. Maue, I. Buettner, M. Richards, U. Chistensen, and U. Keller, *DAWN FC2 CALIBRATED VESTA IMAGES V1.0, DAWN-A-FC2-3-RDR-VESTA-IMAGES-V1.0*. NASA Planetary Data System, 2011.

[40] C. Russell and C. Raymond, *The Dawn Mission to Minor Planets 4 Vesta and 1 Ceres*. Springer, 2012.

[41] D. Scheeres, R. Gaskell, S. Abe, O. Barnouin, T. Hashimoto, J. Kawaguchi, T. Kubota, J. Saito, M. Yoshikawa, N. Hirata, T. Mukai, M. Ishiguro, T. Kominato, K. Shirakawa, and M. Uo, "The *Actual* Dynamical Environment About Itokawa," *AIAA/AAS Astrodynamics Specialist Conference*, Keystone, CO, USA, 2006.

[42] A. Konopliv, S. Asmar, R. Park, B. Bills, F. Centinello, A. Chamberlin, A. Ermakov, R. Gaskell, N. Rambaux, C. Raymond, C. Russell, D. Smith, P. Tricarico, and M. Zuber, "The Vesta gravity field, spin pole and rotation period, landmark positions, and ephemeris from the Dawn tracking and optical data," *Icarus*, Vol. 240, 2014, pp. 103 – 117.

[43] G. S. Chirikjian, *Stochastic Models, Information Theory, and Lie Groups, Volume 2: Analytic Methods and Modern Applications*, Vol. 2. Springer Science & Business Media, 2011.

[44] F. Preusker, F. Scholten, K.-D. Matz, T. Roatsch, R. Jaumann, C. Raymond, and C. Russell, *DAWN FC2 DERIVED VESTA DTM SPG V1.0, DAWN-A-FC2-5-VESTADTMSPG-V1.0*. NASA Planetary Data System, 2016.

[45] W. Hu and D. Scheeres, "Numerical determination of stability regions for orbital motion in uniformly rotating second degree and order gravity fields," *Planetary and Space Science*, Vol. 52, 2004, pp. 685–692.

[46] N. Aspert, D. Santa-Cruz, and T. Ebrahimi, "MESH: Measuring Errors Between Surfaces Using the Hausdorff Distance," *IEEE Intl. Conf. in Multimedia and Expo (ICME)*, Vol. 1, Lausanne, Switzerland, 2002, pp. 705–708.

APPENDIX A: HAUSDORFF DISTANCE

We employ the *bidirectional* Hausdorff distance d_H to obtain a distance metric between the actual shape model and the triangular surface mesh obtained from our shape reconstruction algorithm. The following definitions are adopted from Aspert et al.[46] To obtain this metric, we first define the *one-sided* Hausdorff distance d_O between a point p belonging to a surface $\mathcal{S}$ and a surface $\mathcal{S}'$ as[46]

$$d_O(\mathcal{S}, \mathcal{S}') = \max_{p \in \mathcal{S}} d(p, \mathcal{S}'), \tag{11}$$

where

$$d(p, \mathcal{S}') = \min_{p' \in \mathcal{S}'} \|p - p'\|_2.$$

The bidirectional Hausdorff distance d_H is then defined as[46]

$$d_H(\mathcal{S}, \mathcal{S}') = \max\left\{d_O(\mathcal{S}, \mathcal{S}'), d_O(\mathcal{S}', \mathcal{S})\right\}. \tag{12}$$

Furthermore, the distance metric defined above in Equation (11) can be used to define a mean error d_O^{μ} and root mean square error d_O^{RMS} between the surfaces $\mathcal{S}$ and $\mathcal{S}'$:[46]

$$d_O^{\mu}(\mathcal{S}, \mathcal{S}') = \frac{1}{|\mathcal{S}|} \int\int_{p \in \mathcal{S}} d(p, \mathcal{S}') \, \mathrm{d}S, \tag{13}$$

$$d_O^{\text{RMS}}(\mathcal{S}, \mathcal{S}') = \sqrt{\frac{1}{|\mathcal{S}|} \int\int_{p \in \mathcal{S}} d(p, \mathcal{S}')^2 \, \mathrm{d}S}, \tag{14}$$

where $|\mathcal{S}|$ is the area of $\mathcal{S}$. Bidirectional versions of the mean and root mean square error, d_H^{μ} and d_H^{RMS}, respectively, can be defined using Equation (12).